

Laser-Driven Proton Acceleration Enhancement by Nanostructured Foils

D. Margarone,¹ O. Klimo,^{1,2} I. J. Kim,³ J. Prokūpek,^{1,2} J. Limpouch,^{1,2} T. M. Jeong,³ T. Mocek,¹ J. Pšikal,^{1,2} H. T. Kim,³ J. Proška,² K. H. Nam,³ L. Štolcová,^{1,2} I. W. Choi,³ S. K. Lee,³ J. H. Sung,³ T. J. Yu,³ and G. Korn¹

¹*Institute of Physics of the ASCR, ELI-Beamlines/HiLASE project, Na Slovance 2, 18221 Prague, Czech Republic*

²*Czech Technical University in Prague, FNSPE, Brehova 7, 115 19 Prague, Czech Republic*

³*Advanced Photonics Research Institute, GIST, 1 Oryong-dong, Buk-gu, Gwangju 500-712, Republic of Korea*

(Received 3 June 2012; published 3 December 2012)

Nanostructured thin plastic foils have been used to enhance the mechanism of laser-driven proton beam acceleration. In particular, the presence of a monolayer of polystyrene nanospheres on the target front side has drastically enhanced the absorption of the incident 100 TW laser beam, leading to a consequent increase in the maximum proton energy and beam charge. The cutoff energy increased by about 60% for the optimal spheres' diameter of 535 nm in comparison to the planar foil. The total number of protons with energies higher than 1 MeV was increased approximately 5 times. To our knowledge this is the first experimental demonstration of such advanced target geometry. Experimental results are interpreted and discussed by means of $2\frac{1}{2}$ -dimensional particle-in-cell simulations.

DOI: [10.1103/PhysRevLett.109.234801](https://doi.org/10.1103/PhysRevLett.109.234801)

PACS numbers: 41.75.Jv, 52.38.Ph, 52.50.Dg, 52.59.-f

Recently, the dramatic increase in attainable laser intensity by means of high power femtosecond lasers has generated a fast evolution of laser plasma sources. Production and acceleration of protons up to the 100 MeV level in very small distances (typically a few micrometers) are clearly visible through this evolution [1,2]. A great attention to potential medical application, especially in the hadron therapy [3], has been paid due to the spectacular high brightness, short pulse duration (\sim kA current), and extremely low emittance (100-fold better than typical rf accelerators) of laser-driven ions [4].

Currently the laser acceleration mechanism most investigated experimentally is the so-called target normal sheath acceleration (TNSA) when ions are accelerated at the rear-side of a thin target in a quasioleostatic sheath created by fast electrons propagating from the target front side [5,6], as illustrated in Fig. 1. Theoretically, the possibility to generate monoenergetic ion bunches by accelerating ultra-thin foils using very high contrast circularly polarized laser pulses at intensities higher than 10^{21} W/cm², in the so-called radiation pressure acceleration regime, has been identified [7–9] but not clearly demonstrated experimentally due to the lack of enough powerful lasers, although a first experimental evidence of the laser radiation pressure in a hybrid acceleration regime has been shown [10]. Recently, the acceleration of monoenergetic high energy proton beams by collisionless shocks in gas target has also been demonstrated [11].

Typical TNSA conversion efficiency (ratio between the laser energy and the total ion beam energy) by using 10–100 fs lasers can reach values up to a few percent [12]. However, the laser energy transformation into high energy protons has to be substantially raised for the majority of practical applications. Laser absorption may be boosted by the presence of sub-micrometer-scale structures on the

laser-irradiated target surface, as demonstrated by experiments aimed to enhance the laser energy transformation into x-ray emission [13,14] and photoelectron generation at relatively low laser intensities [15]. Recent particle-in-cell (PIC) simulations have shown that the presence of microstructures with a characteristic size comparable to laser wavelength on the front side of a thin target may significantly increase the energy of hot electrons [16] and of ions emerging from its rear side, assuming a sufficiently high laser contrast [17].

The possibility of using a thin plastic foil covered by a monolayer of polystyrene microspheres with a diameter of the order of the laser wavelength has been studied by PIC simulations [18]. In this Letter we show the first

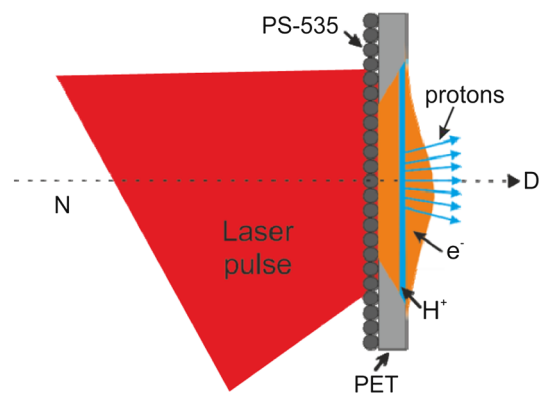


FIG. 1 (color online). TNSA mechanism with the target geometry used in the experiment (side view). The laser beam (p polarized) is absorbed at the nanospheres-vacuum interface with an incidence angle of 22.5 degrees (N denotes the target normal). The hot electrons (generated at the target front side) propagate forward and accelerate protons at the rear side. The proton or ion diagnostics (D) is placed along the N direction.

experimental demonstration of such advanced target geometry which allows us to strongly enhance both the maximum achievable proton energy and total number.

The nanostructured target geometry is depicted in Fig. 1. A monolayer of polystyrene (PS) nanospheres is located at the front-surface of a 1- μm thick mylar [polyethylene terephthalate (PET)] foil. Several targets having different sphere diameters, such as 266, 535, and 920 nm, have been used in our experimental campaign.

The experiment has been performed with the 10 Hz, 100 TW Ti:sapphire laser system at the Advanced Photonics Research Institute in Gwangju, South Korea, which is based on the chirped pulse amplification technique [19]. The laser pulse duration, wavelength, and energy after compression, monitored during the experiment, were about 30 fs (FWHM), 805 nm, and 2 J, respectively. The laser beam was focused onto the target surface by an $f/3.6$ off-axis parabolic mirror, which allowed us to reach a focal spot of about 5 μm in diameter (FWHM). The laser beam was p polarized on target (electric field parallel to the plane of incidence).

The intensity level of the laser nanosecond amplified spontaneous emission is a crucial parameter when using such advanced targets since the nanostructured surface must be preserved to ensure a genuine interaction (no preplasma formation) with femtosecond high-intensity pulses. In fact, we have experimentally estimated the ablation-threshold fluence in the ns regime for the irradiated targets [20], which is in the range of 1–10 J/cm² (corresponding to a laser intensity of about 10⁹ W/cm² in our experimental conditions). Thus, the use of a double plasma mirror, which allowed us to achieve a laser intensity contrast of about 5×10^{11} up to 10 ps prior to the main pulse, was mandatory [21]. On the other hand, the laser pulse energy was reduced by a factor of 50% (about 1 J) on target at the expense of the laser intensity which finally was about 5×10^{19} W/cm².

The standard real-time ion diagnostics used consists of a Thomson parabola (TP) spectrometer and a time-of-flight (TOF) detector fully described in the literature [22]. The TP is a mass spectrograph where charged particles are deflected by static electric and magnetic fields parallel to each other and perpendicular to the particle stream motion; as a result of the laws of motion the particles draw different parabolas on an imaging plane. The TOF detector is based on the well known time-of-flight technique, which allows us to estimate the particle velocity (energy) by measuring the particle arrival time onto a detector placed at a given distance from the source (thin foil in our experiment).

The spectrometer was equipped with a microchannel plate (MCP) and a phosphor screen placed 20 cm away from the output of the magnetic (~ 0.2 T) and electric (3.5 kV/cm) field deflection region, and an ICCD camera. The calibration of the MCP-phosphor screen-ICCD system was performed by installing slotted CR-39 track detectors

in front of the MCP following a similar experimental procedure reported in literature [23]. The TOF consisted of a plastic scintillator (placed at 283 cm from the plasma source), photomultiplier tube and fast oscilloscope. Both detectors were placed along the target normal and allowed us to perform simultaneous measurements (a small hole was located in the center of the scintillator to let ions go through and reach the TP spectrometer). The detection solid angles were 7.2×10^{-9} sr and 2.55×10^{-4} sr for the TP spectrometer and the TOF system, respectively.

Typical signals from TP and TOF measurements are shown in Fig. 2. Since the main target constituents are hydrogen and carbon, the strongest plasma ion products are protons and C^{n+} ($1 \leq n \leq 6$) as clearly shown in the TP spectrum. A comparison between TP and TOF signals has been performed in order to accurately determine the proton energy distribution, proton cutoff energy, and total ion charge. The proton beam divergence (i.e., the proton stream solid angle) was measured by a stack of CR39 track detectors placed near the target. This *ex-situ* diagnostic technique, performed for all configurations (i.e., for all targets with different nanosphere diameters and for all plane-foil targets of different thicknesses), has been used to estimate the total number of protons, taking into account that protons with different energy range have a different divergence.

The proton energy distributions were compared to numerical results coming out from $2\frac{1}{2}$ -dimensional particle-in-cell simulations (with two spatial and three velocity components). The simulations assumed the same laser pulse intensity, wavelength, duration, polarization, and incidence angle used in the experiment. The target

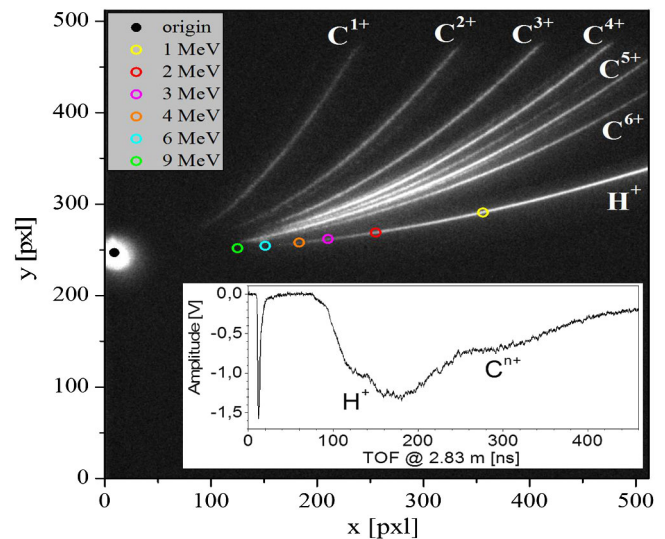


FIG. 2 (color online). TP and TOF typical spectra acquired simultaneously during irradiation of a PET-535 (1 μm thick polyethylene with 535 nm diameter polystyrene spheres) target. The circles from the right to the left hand side show increasing proton energies.

geometry was also the same and the target consisted of 1:1 mixture of C^{4+} ions and protons with electron density 40 times the critical density ($1.72 \times 10^{21} \text{ cm}^{-3}$ for 800 nm wavelength of a Ti:sapphire laser). The transverse intensity distribution of the laser pulse was a Gaussian profile with a spot size of about 2 microns at FWHM [24]. The lateral losses are only one directional in 2D geometry used in simulations and thus they are reduced compared to the experiment. In order to compensate for this reduction, we have used a smaller focal spot in 2D simulations. This spot size in two dimensions has been estimated assuming that the density of hot electrons on the characteristic distance of ion acceleration ($d = \tau_l c_s$, where τ_l is the laser pulse duration and c_s the ion acoustic velocity) should be comparable to the one in three dimensions. The size of the hot electron cloud at a distance d is $2s = 2(d + l) \tan(\alpha) + 2r$, where α is the electron divergence, l is the target thickness, and r is the focal spot radius. Thus, in a first approximation, we can assume that $s_1/r_1 = s_2^2/r_2^2$ (the density in two dimensions is s_1/r_1 times smaller and in three dimensions is s_2^2/r_2^2 times smaller, when compared with an electron stream propagating without any divergence). Finally, assuming a hot electron temperature of 1 MeV and electron divergence of 45° estimated from PIC simulations for the above given parameters and supported by similar results reported in Ref. [18], a foil thickness $l = 1 \mu\text{m}$, and $r_2 = 2.5 \mu\text{m}$ (given as experimental parameter, where the diameter $2r_2$ is assumed as focal spot size at FWHM), we have estimated $r_1 = 1.0 \mu\text{m}$. Nevertheless, we have also performed numerical simulation with the same focal spot diameter as in the experiment ($5 \mu\text{m}$) for all target geometries. The results predicted about 50% higher proton cutoff energies with respect to the case of lower spot size ($2 \mu\text{m}$) at constant laser intensity. The ratio of the maximum proton energies for different target geometries is practically constant in our PIC simulations when different spot sizes are used as inputs. Hence, the numerical results are qualitatively the same for various spot sizes, even if the absolute values differ.

The comparison for the irradiated targets without (PET) and with PS nanospheres (PET-266, PET-535, PET-920) on the front surface is reported in Fig. 3. The best acceleration performances during the experiment were achieved with the PET-535 target. The maximum proton energy measured by the TP spectrometer was about 8.6 MeV [Fig. 3(a)], showing a perfect agreement with the predicted PIC simulations [Fig. 3(b)]. The cutoff energy measured for the planar target (PET) was about 5.3 MeV, also showing a very good agreement with the simulation results. In general, the PIC calculations show a trend for different target geometries which is in agreement with the experimental results. However, the experimental cutoff energy in the case of the PET-920 and PET-266 targets was lower than the calculated ones, probably ascribable to the presence of surface inhomogeneities which has been identified

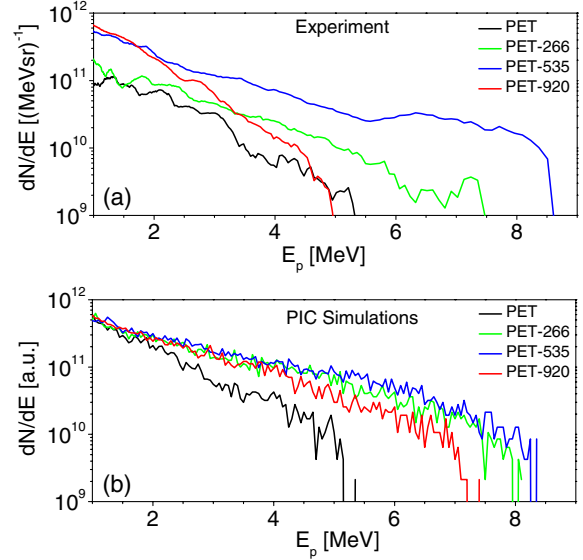


FIG. 3 (color online). Proton energy distributions from analysis of TP spectra (a) and PIC simulations (b) for different irradiated targets. The vertical axis in (b) was rescaled in order to match the experimental values. The experimental cutoff energy for PET, PET-266, PET-535, PET-920 is 5.3, 5, 7.5, and 8.6 MeV, respectively. The PIC simulation cutoff energy for PET, PET-266, PET-535, PET-920 is 5.2, 7.2, 8, and 8.4 MeV, respectively.

(only in the case of these two target geometries) scanning the target surface by scanning electron microscope after the fabrication process.

An accurate statistics has been performed in the experimental campaign and results are summarized in Fig. 4. Both experimental results and numerical simulations show that under optimal experimentally achievable acceleration conditions optimal proton maximum energy as well as total proton beam energy can be obtained when targets with 535 nm diameter spheres are used. Also the total ion energy (estimated from TOF spectra) shows a similar trend (blue dotted line in Fig. 4). The average proton cutoff energy (measured by the TP spectrometer) is about 7.5 and 4.7 MeV for PET-535 (nanostructured target) and PET (planar target), respectively. The average experimental cutoff energy in the case of a $1.5 \mu\text{m}$ thick PET planar target was $(3 \pm 0.6) \text{ MeV}$ (green square in Fig. 4). Results obtained with 535 nm diameter spheres showed a total proton beam energy (ε_p) and ion beam energy (ε_i) which was increased by 6.3 and 3.9 times (average values), respectively, in comparison to the planar target geometry (ε_p^o and ε_i^o). The relatively large experimental error bars reported in the plot are ascribable to the nonideal uniformity of the PS nanospheres on the sample surface and to the fluctuations in the measured proton beam divergence (energy dependent).

The proton cutoff energy and the total beam energy measured in the whole experimental campaign have been

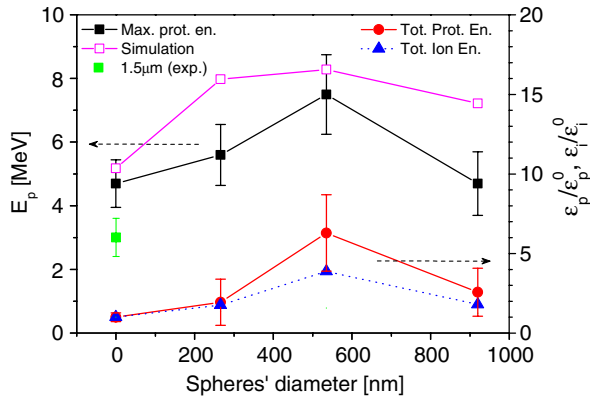


FIG. 4 (color online). Proton beam maximum energy (left-handed axis) and the total energy of the proton and ion beams, each normalized to the case of a planar foil (right-handed axis) for different target geometries.

correlated and plotted in Fig. 5 along with the simulation outputs (hollow symbols). The points for individual experimental shots clearly demonstrate the shot consistency and the growth of the total beam energy with the proton maximum energy, which implies a growth of the acceleration mechanism efficiency. The PIC simulation outputs reported in Fig. 5 also show an increase in the acceleration efficiency (proton cutoff energy and total energy) from a structured target (PET-535) with respect to a planar one (PET), when a similar geometry is used with Petawatt (PW)-class lasers (hollow stars).

The experimental results presented here clearly demonstrate that the use of nanostructured thin plastic foils on the target front side can strongly enhance the laser-driven proton beam acceleration mechanism. In fact, the maximum proton energy was increased by a factor of 1.6 ($\sim 60\%$ increment) for the optimal spheres' diameter of 535 nm in comparison to the planar foil. The effective target thickness did not play a crucial role in the cutoff

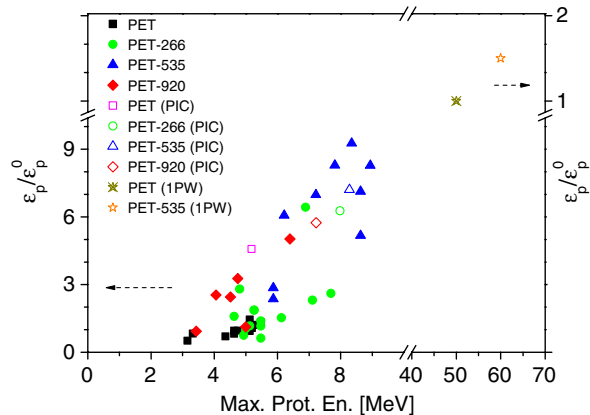


FIG. 5 (color online). Correlation between maximum proton energy and total proton energy in the spectrometer solid angle (full symbols are experimental points and hollow symbols are PIC simulation outputs).

proton energy, in fact in the best case a value of 3.8 MeV was achieved with a 1.5 μm thick PET planar target, which is much lower than the maximum proton energy measured in the case of the 0.9 μm thick PET planar target (about 5 MeV). The total number of protons (with energies exceeding 1 MeV) was increased about 5 times. This valuable experimental result implies a substantial increase in the laser-driven proton acceleration efficiency (about 6 times) that is mainly related to the enhancement of the laser absorption efficiency at the target front surface and to the subsequent increase of the hot electron population, which in turn is responsible for the proton acceleration mechanism [10–15].

The use of an ultrahigh laser contrast ($> 5 \times 10^{11}$) was crucial to ensure a genuine laser-nanosphere interaction allowing the experimental achievement of such enhanced TNSA regime. The slight disagreement between experimental and numerical results in the case of targets with 266 and 920 nm spheres' diameter can be ascribed to nonuniformities on the target surface detected after the target fabrication, which practically reduce the effective interaction of the laser beam with the structured surface (the number of nanospheres in the laser spot area is lower than the one used in our simulations).

A number of different effects may contribute to higher absorption for the used nanostructured targets. In fact, the nanosphere layer on the target front side implies an effective larger surface area; i.e., a higher number of particles can interact with the laser field. Moreover, the nanosphere screens the incident laser wave but the accelerated electrons can propagate through it, and, consequently, be easily out of the laser wave phase, thus gaining energy more efficiently along the longitudinal direction. This absorption process can be associated with the multipass stochastic heating in the case of laser interaction with clusters [25]. Unlike the case of laser coupling to a surface wave, where a resonant matching of the laser incidence angle and the structure period is required [16], the PIC simulations show that both the laser absorption and the proton acceleration efficiency are not particularly sensitive to the laser incidence angle [18]. However, along the experiment the laser incidence angle was not normal (with respect to the target surface); thus, vacuum heating [26] and resonance absorption [27] mechanisms might have played a role. Since the latter parameter has not been optimized during our experimental campaign (it was kept constant at 22.5° due to experimental constraints), the increase in TNSA acceleration efficiency might be further improved in future experiments.

The complex interplay of the above discussed physical mechanisms can lead to the experimental and numerical achievements reported here (similar results were presented in our previous theoretical paper [18]) showing an optimal target geometry (in terms of maximum proton energy and total number) in the case of spheres with a diameter of

535 nm. This results can be qualitatively explained in a very simplified picture: the 920 nm spheres are too large (too far each other) to maximize the collective interaction among the laser field and electrons belonging to neighboring spheres and a sort of “photon scattering” occurs; the 266 nm spheres are too small (too close each other) and a sort of “smoothing” in the collective interaction occurs leading to a condition similar to the case of a planar surface target. A similar result is reported in Ref. [14] where the highest x-ray yield (corresponding to an optimal laser absorption) is achieved for a sphere diameter slightly larger than half the laser wavelength (260 nm for a 400 nm wavelength in Ref. [14] and 535 nm for a 805 nm in our experiment).

Moreover, fine structures comparable to the laser spot size, e.g., microdots, might be additionally added on the target rear side in order to improve the energetic and/or angular characteristics of the accelerated ion bunches [28,29]. Such enhanced photo-proton sources may be considered as a compact alternative to low energy large conventional accelerators with a possible use for cancer therapy or other applications. In fact, our simulations show that a maximum proton energy of about 60 MeV (requested energy for eye melanoma treatment [30]) can be reached when using a PW-class laser beam with an intensity of about 2×10^{21} W/cm² (nominally 0.5 PW on target and 5 μ m focal spot diameter) on the investigated nano-structured samples. The PIC simulations show that the maximum proton energy is also increased in this laser intensity regime (about 20%) as reported in Fig. 5.

This work benefitted from the support of the Czech Science Foundation (Project No. P205/11/1165), the Czech Republic’s Ministry of Education, Youth and Sports to the HiLASE (CZ.1.05/2.1.00/01.0027), ELI-Beamlines (CZ.1.05/1.1.00/483/02.0061) and OPVK (CZ.1.07/2.3.00/20.0087) projects, the Academy of Sciences of the Czech Republic (M100101210 and KAN401220801), the CHARPAC Work Package of the Laserlab-Europe III (Project No. 284464), the Czech Technical University in Prague (RVO68407700) and the Ministry of Knowledge and Economy of Korea through the Ultrashort Quantum Beam Facility Project. Authors also thank Dr. J. Krasa, Dr. L. Laska, Dr. K. Jungwirth, and Professor S. V. Bulanov for the useful scientific discussions and Mr. S. W. Kang for the valuable technical support along the experiment.

[1] R. A. Snavely *et al.*, *Phys. Rev. Lett.* **85**, 2945 (2000).
 [2] M. Borghesi, A. Schiavi, D. H. Campbell, M. G. Haines, O. Willi, A. J. MacKinnon, L. A. Gizzi, M. Galimberti, R. J. Clarke, and H. Ruhl, *Plasma Phys. Control. Fusion* **43**, A267 (2001).

[3] V. Malka, J. Faure, Y. A. Gauduel, E. Lefebvre, A. Rousse, and K. T. Phuoc, *Nat. Phys.* **4**, 447 (2008).
 [4] T. E. Cowan *et al.*, *Phys. Rev. Lett.* **92**, 204801 (2004).
 [5] S. P. Hatchett *et al.*, *Phys. Plasmas* **7**, 2076 (2000).
 [6] S. C. Wilks, A. B. Langdon, T. E. Cowan, M. Roth, M. Singh, S. Hatchett, M. H. Key, D. Pennington, A. MacKinnon, and R. A. Snavely, *Phys. Plasmas* **8**, 542 (2001).
 [7] T. Esirkepov, M. Borghesi, S. V. Bulanov, G. Mourou, and T. Tajima, *Phys. Rev. Lett.* **92**, 175003 (2004).
 [8] A. Macchi, F. Cattani, T. V. Liseykina, and F. Cornolti, *Phys. Rev. Lett.* **94**, 165003 (2005).
 [9] B. Qiao, S. Kar, M. Geissler, P. Gibbon, M. Zepf, and M. Borghesi, *Phys. Rev. Lett.* **108**, 115002 (2012).
 [10] A. Henig *et al.*, *Phys. Rev. Lett.* **103**, 245003 (2009).
 [11] D. Haberberger, S. Tochitsky, F. Fiuza, C. Gong, R. A. Fonseca, L. O. Silva, W. B. Mori, and C. Joshi, *Nat. Phys.* **8**, 95 (2012).
 [12] Y. Sentoku, T. E. Cowan, A. Kemp, and H. Ruhl, *Phys. Plasmas* **10**, 2009 (2003).
 [13] T. Nishikawa, H. Nakano, K. Oguri, N. Uesugi, K. Nishio, and H. Masuda, *J. Appl. Phys.* **96**, 7537 (2004).
 [14] H. A. Sumeruk, S. Kneip, D. R. Symes, I. V. Churina, A. V. Belolipetski, T. D. Donnelly, and T. Ditmire, *Phys. Rev. Lett.* **98**, 045001 (2007).
 [15] M. Raynaud and J. Kupersztich, *Phys. Rev. B* **76**, 241402 (2007).
 [16] M. Raynaud, J. Kupersztich, C. Riconda, J. C. Adam, and A. Heron, *Phys. Plasmas* **14**, 092702 (2007).
 [17] Y. Nodera, S. Kawata, N. Onuma, J. Limpouch, O. Klimo, and T. Kikuchi, *Phys. Rev. E* **78**, 046401 (2008).
 [18] O. Klimo, J. Psikal, J. Limpouch, J. Proska, F. Novotny, T. Ceccotti, V. Floquet, and S. Kawata, *New J. Phys.* **13**, 053028 (2011).
 [19] T. M. Jeong *et al.*, *J. Korean Phys. Soc.* **50**, 34 (2007).
 [20] D. Margarone, A. Velyhan, L. Torrisi, M. Cutroneo, L. Giuffrida, A. Picciotto, J. Krasa, S. Cavallaro, J. Limpouch, O. Klimo, J. Psikal, J. Proska, and F. Novotny, *Appl. Surf. Sci.* (in press).
 [21] I. J. Kim, I. W. Choi, S. K. Lee, K. A. Janulewicz, J. H. Sung, T. J. Yu, H. T. Kim, H. Yun, T. M. Jeong, and J. Lee, *Appl. Phys. B* **104**, 81 (2011).
 [22] I. W. Choi *et al.*, *Rev. Sci. Instrum.* **80**, 053302 (2009).
 [23] R. Prasad *et al.*, *Nucl. Instrum. Methods Phys. Res., Sect. A* **623**, 712 (2010).
 [24] J. Psikal, J. Limpouch, S. Kawata, and A. A. Andreev, *Czech. J. Phys.* **56**, B515 (2006).
 [25] B. N. Breizman, A. V. Arefiev, and M. V. Fomyts’kyi, *Phys. Plasmas* **12**, 056706 (2005).
 [26] F. Brunel, *Phys. Rev. Lett.* **59**, 52 (1987).
 [27] W. L. Kruer, *The Physics of Laser Plasma Interactions* (Addison-Wesley, Reading, MA, 1988).
 [28] H. Schwoerer, S. Pfoth, O. Jäckel, K.-U. Amthor, B. Liesfeld, W. Ziegler, R. Sauerbrey, K. W. D. Ledingham, and T. Esirkepov, *Nature (London)* **439**, 445 (2006).
 [29] K. Takahashi, S. Kawata, D. Satoh, Y. Y. Ma, D. Barada, Q. Kong, and P. X. Wang, *Phys. Plasmas* **17**, 093102 (2010).
 [30] G. Cuttone *et al.*, *Eur. Phys. J. Plus* **126**, 65 (2011).